Modeling of a Multi-Phase Bearingless Surface Permanent Magnet Synchronous Machine in Stationary and Synchronous Coordinates

Dennis GUHL* and Wilfried HOFMANN*
* TU Dresden
Helmholtzstrasse 9, 01069 Dresden, Germany
E-mail: dennis.guhl@tu-dresden.de

Abstract
Multi-phase bearingless machines offer enhanced fault tolerance and flexible power distribution between force and torque generation. Recent research efforts have focused on winding design methodologies and advanced force modeling incorporating higher harmonic effects. This work presents a compact linear analytical motor model for bearingless machines with surface permanent magnets. The model covers both stationary and synchronous reference frames while incorporating higher harmonics and rotor eccentricity effects. The derived analytical expressions can be used during the design process to identify necessary fundamental design parameters as well as critical influence quantities on torque and force ripple. They also provide parameters directly implementable for control system design. Finite element method simulations validate the accuracy and applicability of the proposed analytical formulations.

Keywords : Bearingless Motor, Multi-Phase Machine, Machine Model, Eccentricity, Higher Harmonics

1. Introduction

Multi-phase machines are increasingly gaining attention in industrial applications demanding frictionless and fault-tolerant operation. For bearingless motors, a multi-phase design offers the dual advantage of simultaneously generating force and torque, alongside flexible power distribution. However, this comes at the cost of increased system complexity, as the dimensionality scales with the number of phases. Recent research has sought to address this complexity. For instance, Loewenherz (Loewenherz et al., 2020) proposed simplified modeling approaches utilizing semi-analytical FEM investigations, while Khamitov and Severson (Khamitov and Severson, 2025) introduced an improved multi-harmonic force vector model that accounts for the effects of multiple current systems with adjacent sequences and higher space harmonics. Building upon these foundations, this paper presents a compact linear, analytical model for multi-phase bearingless motors in both stationary and synchronous coordinate systems also considering the impact of rotor eccentricity throughout.
The paper is structured as follows: Section 2 introduces the investigated motor, Section 3 presents the electromagnetic and mechanical model, Sections 4 to 7 derive parameter formulas, and Section 8 validates results against FEM simulations.

2. Investigated Motor

The investigated machine was a conventional three-phase industrially available spindle motor from (Guhl, Liebfried, and Hofmann, 2021) as the new bearingless design shall be used to dampen chatter vibrations. It had a double-layer 7/9 short-pitched winding with four parallel branches per phase. Only changes to the stator winding were made. The previously parallelized coil groups now each represent one single phase. Table 1 lists the main design parameters.

Table 1: Investigated bearingless spindle motor specifications

symbol	quantity	value	symbol	quantity	value	symbol	quantity	value
P_N	nominal power	25 kW	l_Fe	axial length	80 mm	N	number of slots	36
n_N	nominal speed	10000 rpm	$r_\mathrm{s\,i}$	inner radius stator	40 mm	q	no. of slots per phase	3
I_N	nominal current	13.75 A	δ_0	mech. airgap	2.5 mm	y	coil span	7
m	phase number	12	h_PM	magnet height	3.5 mm	w	number of turns	45
p	pole pairs	2	α_p	pole coverage	1	ξ_p	motor winding factor	0.9
p_s	susp. pole pairs	3				$\xi_{\mathrm{p_s}}$	susp. winding factor	0.88
—	steel material	M270-35A	$B_\mathrm{rem\,PM}$	remanence flux density	1.29 T	$\mu_\mathrm{r\,PM}$	rel. permeability PM	1.05

3. Motor model

As a first step, a general electromagnetic and mechanical model is developed using vector-matrix notation (**bold** values are non-scalar) for multi-phase machine theory. Starting from the voltage equations for each of the m phases

$$\boldsymbol{u}_{\mathrm{ph}} = R_{\mathrm{s}}\boldsymbol{i}_{\mathrm{ph}} + \dot{\boldsymbol{\Psi}}_{\mathrm{ph}}, \tag{1}$$

the transformation into synchronous coordinates via the amplitude invariant transformation matrix $\boldsymbol{T}_{\mathrm{dq0}}$ leads to

$$\boldsymbol{u}_{\mathrm{dq0}} = R_{\mathrm{s}}\boldsymbol{i}_{\mathrm{dq0}} + \boldsymbol{W}\boldsymbol{\Psi}_{\mathrm{dq0}} + \dot{\boldsymbol{\Psi}}_{\mathrm{dq0}}; \qquad \boldsymbol{W} = \mathrm{diag}(\boldsymbol{W}_1, \boldsymbol{W}_1, \ldots, \boldsymbol{W}_1, \boldsymbol{0}) \in \mathbb{R}^{m\times m}; \qquad \boldsymbol{W}_1 = \begin{bmatrix} 0 & -\omega \\ \omega & 0 \end{bmatrix}, \tag{2}$$

with the coupling matrix $\boldsymbol{W}$ and the zero matrix $\boldsymbol{0}$. Each pair of rows accounts for one of the $\lceil m/2 \rceil - 1$ orthogonal dq-systems of ascending order k, corresponding to a fundamental field wave of the same periodicity. The last or the last two rows account for the zero components ("d0": dc-component, "q0": homopolar component). The flux linkages generally depend on the stator currents $\boldsymbol{i}_{\mathrm{dq0}}$, the electric rotation angle θ and the rotor position $\boldsymbol{x} = [x, y]^{\mathrm{T}}$. Using the total derivative and dividing the total flux linkage into a part from the permanent magnets and a part from the winding $\boldsymbol{\Psi}_{\mathrm{dq0}} = \boldsymbol{L}_{\mathrm{dq0}}\boldsymbol{i}_{\mathrm{dq0}} + \boldsymbol{\Psi}_{\mathrm{PM\,dq0}}$, the extended voltage equations are obtained as

$$\boldsymbol{u}_{\mathrm{dq0}} = R_{\mathrm{s}}\boldsymbol{i}_{\mathrm{dq0}} + \boldsymbol{W}\left(\boldsymbol{L}_{\mathrm{dq0}}\boldsymbol{i}_{\mathrm{dq0}} + \boldsymbol{\Psi}_{\mathrm{PM\,dq0}}\right) + \omega\boldsymbol{\Upsilon}_{\mathrm{dq0}\,\theta} + \boldsymbol{\mathcal{L}}_{\mathrm{dq0}}\frac{\mathrm{d}\boldsymbol{i}_{\mathrm{dq0}}}{\mathrm{d}t} + \boldsymbol{\Gamma}_{\mathrm{dq0\,xy}}\frac{\mathrm{d}\boldsymbol{x}}{\mathrm{d}t}, \tag{3}$$

where $\boldsymbol{L}_{\mathrm{dq0}}$ is the absolute inductance matrix, $\boldsymbol{\Psi}_{\mathrm{PM\,dq0}}$ the PM flux linkage, $\boldsymbol{\mathcal{L}}_{\mathrm{dq0}} = \frac{\partial\boldsymbol{\Psi}_{\mathrm{dq0}}}{\partial\boldsymbol{i}_{\mathrm{dq0}}}$ the differential inductance matrix, $\boldsymbol{\Upsilon}_{\mathrm{dq0}\,\theta} = \frac{\partial\boldsymbol{\Psi}_{\mathrm{dq0}}}{\partial\theta}$ the differential angle dependencies and $\boldsymbol{\Gamma}_{\mathrm{dq0\,xy}} = \frac{\partial\boldsymbol{\Psi}_{\mathrm{dq0}}}{\partial\boldsymbol{x}}$ the differential position dependencies. Assuming current independent inductances, the differential inductance matrix is equal to the absolute one.

The mechanical model is based on the Maxwell stress tensor. Formulas for torque and force are therefore expressed via the radial and tangential magnetic flux densities $B_{\mathrm{r}}(r_{\mathrm{s\,i}}, \alpha)$ resp. $B_{\mathrm{t}}(r_{\mathrm{s\,i}}, \alpha)$ at the inner stator bore

$$T = \frac{l_{\mathrm{i}}r_{\mathrm{s\,i}}}{\mu_0}\int_0^{2\pi} B_{\mathrm{r}}(r_{\mathrm{s\,i}}, \alpha)B_{\mathrm{t}}(r_{\mathrm{s\,i}}, \alpha)\mathrm{d}\alpha; \qquad \boldsymbol{F} = \frac{l_{\mathrm{i}}r_{\mathrm{s\,i}}}{2\mu_0}\int_0^{2\pi}\begin{bmatrix} B_{\mathrm{r}}^2(r_{\mathrm{s\,i}}, \alpha)\cos(\alpha) - 2B_{\mathrm{r}}(r_{\mathrm{s\,i}}, \alpha)B_{\mathrm{t}}(r_{\mathrm{s\,i}}, \alpha)\sin(\alpha) \\ B_{\mathrm{r}}^2(r_{\mathrm{s\,i}}, \alpha)\sin(\alpha) - 2B_{\mathrm{r}}(r_{\mathrm{s\,i}}, \alpha)B_{\mathrm{t}}(r_{\mathrm{s\,i}}, \alpha)\cos(\alpha) \end{bmatrix}\mathrm{d}\alpha, \tag{4}$$

where α denotes the airgap angle and l_{i} the effective axial length. We assume that the airgap field, formed by a radial and tangential part, consists of the permanent magnet field density $\boldsymbol{B}_{\mathrm{PM}}$, the torque producing stator field resp. motor field density $\boldsymbol{B}_{\mathrm{m}}$ and the force producing stator field resp. suspension field density $\boldsymbol{B}_{\mathrm{s}}$

$$\boldsymbol{B} = \begin{bmatrix} B_{\mathrm{r}} \\ B_{\mathrm{t}} \end{bmatrix} = \boldsymbol{B}_{\mathrm{PM}} + \boldsymbol{B}_{\mathrm{m}} + \boldsymbol{B}_{\mathrm{s}} = \begin{bmatrix} B_{\mathrm{PM\,r}} + B_{\mathrm{m\,r}} + B_{\mathrm{s\,r}} \\ B_{\mathrm{PM\,t}} + B_{\mathrm{m\,t}} + B_{\mathrm{s\,t}} \end{bmatrix}. \tag{5}$$

The resulting torque and force equations can be found in (Guhl and Hofmann, 2024). They assume a machine without any reluctance differences in the rotor. The tangential PM field component can be neglected at the stator bore as the PMs are radially magnetized and therefore the fundamental amplitude is significantly lower than the ones of the motor and suspension field.

4. Airgap winding field

The airgap winding field density $\boldsymbol{B}_{\mathrm{w}}$ depends on the stator currents, the electrical angle of rotation, and the rotor position. The latter dependency is particularly relevant for bearingless motors. Considerable changes can occur depending on the ratio of the rotor's eccentricity from the center position to the magnetically effective airgap. The linear method presented below for modeling flux densities in the airgap, and thus the inductances, provides a compact analytical description that enables simple identification of the rotor position's influence. The winding axis of phase A is aligned with the global x-axis.

4.1. Radial field component

The radial field density component $B_{\mathrm{w\,r}}$ is calculated according to (Faiz and Tabatabaei, 2002) as follows:

$$B_{\mathrm{w\,r}}(\alpha, \boldsymbol{i}_{\mathrm{ph}}, \boldsymbol{x}) = \mu_0\sum_{a=1}^{m} N_a(\alpha, \boldsymbol{x})P(\alpha, \boldsymbol{x})i_a(\omega t); \qquad N_a(\alpha, \boldsymbol{x}) = n_a(\alpha) - \frac{\int_0^{2\pi} n_a(\alpha)\,P(\alpha, \boldsymbol{x})\mathrm{d}\alpha}{\int_0^{2\pi} P(\alpha, \boldsymbol{x})\mathrm{d}\alpha}, \tag{6}$$

where n_a is the winding function with the coefficients $\hat{n}_\nu$, P is the inverse of the effective airgap δ_{i}

$$\delta_{\mathrm{i}}(\alpha, \boldsymbol{x}) = k_{\mathrm{c}}\left(\delta_0 + \frac{h_{\mathrm{PM}}}{\mu_{\mathrm{r\,PM}}} - x\cos(\alpha) - y\sin(\alpha)\right) = k_{\mathrm{c}}\left(\delta_0' - x\cos(\alpha) - y\sin(\alpha)\right), \tag{7}$$

which can be approximated by a first order Taylor expansion, and N_a is the modified winding function

$$N_a(\alpha, \boldsymbol{x}) = \sum_{\nu=1}^{\infty}\left[\hat{n}_\nu \cos\left(\nu\left(\alpha-(a-1)\frac{2\pi}{m}\right)\right)\right] - \frac{\hat{n}_1}{2}\left(\frac{x}{\delta_0'}\cos\left((a-1)\frac{2\pi}{m}\right)+\frac{y}{\delta_0'}\sin\left((a-1)\frac{2\pi}{m}\right)\right). \tag{8}$$

Thus, for a centered rotor, it equals the winding function adjusted for its mean value. The Carter's factor k_c accounts for the stator slotting. A radial dependency is not considered in (Faiz and Tabatabaei, 2002), but as the investigated machine has surface PMs and therefore a large mechanical airgap, this needs to be added. Zhu and Howe introduce a curvature coefficient $\xi_{\mathrm{r}\nu}$ in (Zhu and Howe, 1993:p. 137). However, it is only valid for a centered rotor. Due to the Taylor approximation of the inverse airgap, the radial field density component in Eq. (6) can be split into a eccentricity-independent part $B_{\mathrm{w\,r\,cent}}$ and a eccentricity-dependent part $B_{\mathrm{w\,r\,xy}}$ while the curvature coefficient is only valid for the former.

$$\begin{aligned}
&B_{\mathrm{w\,r}}(\alpha, r, \boldsymbol{i}_\mathrm{ph}\,\boldsymbol{x}) = B_{\mathrm{w\,r\,cent}}(\alpha, r, \boldsymbol{i}_\mathrm{ph}) + B_{\mathrm{w\,r\,xy}}(\alpha, \boldsymbol{i}_\mathrm{ph}, \boldsymbol{x}) = \\
&= \frac{\mu_0}{k_\mathrm{c}\delta_0'}\sum_{a=1}^{m}\Bigg[\sum_{\nu=1}^{\infty}\Bigg[\xi_{\mathrm{r}\nu}(r)\hat{n}_\nu\cos\left(\nu\left(\alpha-(a-1)\frac{2\pi}{m}\right)\right)+\frac{\hat{n}_\nu}{2}\Bigg[\frac{x}{\delta_0'}\left[\cos\left(\alpha(\nu-1)-\nu(a-1)\frac{2\pi}{m}\right)+\cos\left(\alpha(\nu+1)-\nu(a-1)\frac{2\pi}{m}\right)\right]+ \\
&+\frac{y}{\delta_0'}\left[-\sin\left(\alpha(\nu-1)-\nu(a-1)\frac{2\pi}{m}\right)+\sin\left(\alpha(\nu+1)-\nu(a-1)\frac{2\pi}{m}\right)\right]\Bigg]\Bigg]-\frac{\hat{n}_1}{2}\left[\frac{x}{\delta_0'}\cos\left((a-1)\frac{2\pi}{m}\right)+\frac{y}{\delta_0'}\sin\left((a-1)\frac{2\pi}{m}\right)\right]\Bigg]i_a
\end{aligned} \tag{9}$$

The last summand guarantees that there is no DC component when $\nu = 1$. A rotor eccentricity leads to additional harmonics whose orders differ by one from existing harmonic orders. These results in force effects and should be considered in the mechanical modeling. The radial field component can also be expressed as a function of a fundamental symmetrical current system $\boldsymbol{i}_k$ of sequence k with the amplitude $\hat{i}_k$ and the phase shift $\varphi_{\mathrm{i}\,k}$:

$$B_{\mathrm{w\,r\,cent}}(\alpha, r, \boldsymbol{i}_k) = \frac{m}{2}\frac{\mu_0}{k_\mathrm{c}\delta_0'}\hat{i}_k\left[\sum_{\nu=gm-k>0}^{\infty}\xi_{\mathrm{r}\nu}\hat{n}_\nu\cos\left(\nu\alpha+\omega t+\varphi_{\mathrm{i}\,k}\right)+\sum_{\nu=gm+k>0}^{\infty}\xi_{\mathrm{r}\nu}\hat{n}_\nu\cos\left(\nu\alpha-\omega t-\varphi_{\mathrm{i}\,k}\right)\right] \quad ; g\in\mathbb{N}_0 \tag{10a}$$

$$\begin{aligned}
B_{\mathrm{w\,r\,xy}}(\alpha, \boldsymbol{i}_k, \boldsymbol{x}) = \frac{m}{4}\frac{\mu_0}{k_\mathrm{c}\delta_0'}\hat{i}_k\Bigg[&\sum_{\nu=gm-k-1>0}^{\infty}\hat{n}_{\nu+1}\left[\frac{x}{\delta_0'}\cos\left(\alpha\nu+\omega t+\varphi_{\mathrm{i}\,k}\right)-\frac{y}{\delta_0'}\sin\left(\alpha\nu+\omega t+\varphi_{\mathrm{i}\,k}\right)\right] \\
&+\sum_{\nu=gm-k+1>0}^{\infty}\hat{n}_{\nu-1}\left[\frac{x}{\delta_0'}\cos\left(\alpha\nu+\omega t+\varphi_{\mathrm{i}\,k}\right)+\frac{y}{\delta_0'}\sin\left(\alpha\nu+\omega t+\varphi_{\mathrm{i}\,k}\right)\right]+ \\
&+\sum_{\nu=gm+k-1>0}^{\infty}\hat{n}_{\nu+1}\left[\frac{x}{\delta_0'}\cos\left(\alpha\nu-\omega t-\varphi_{\mathrm{i}\,k}\right)-\frac{y}{\delta_0'}\sin\left(\alpha\nu-\omega t-\varphi_{\mathrm{i}\,k}\right)\right]+ \\
&+\sum_{\nu=gm+k+1>0}^{\infty}\hat{n}_{\nu-1}\left[\frac{x}{\delta_0'}\cos\left(\alpha\nu-\omega t-\varphi_{\mathrm{i}\,k}\right)+\frac{y}{\delta_0'}\sin\left(\alpha\nu-\omega t-\varphi_{\mathrm{i}\,k}\right)\right]\Bigg].
\end{aligned} \tag{10b}$$

4.2. Tangential field component

The tangential component of the airgap winding field density $B_{\mathrm{w\,t}}$ results at the stator bore directly from the current loading A

$$B_{\mathrm{w\,t}}(\alpha, \boldsymbol{i}_\mathrm{ph}, r_{\mathrm{S\,i}}) = \mu_0 H_{\mathrm{w\,t}}(\alpha, \boldsymbol{i}_\mathrm{ph}, r_{\mathrm{S\,i}}) = \mu_0 A(\alpha, \boldsymbol{i}_\mathrm{ph}). \tag{11}$$

The current loading can generally be expressed as a function of the individual phase currents $\boldsymbol{i}_\mathrm{ph}$ or directly as a function of a fundamental symmetrical current system $\boldsymbol{i}_k$.

$$A(\alpha, \boldsymbol{i}_\mathrm{ph}) = \sum_{a=1}^{m}\sum_{\nu=1}^{\infty}-\frac{4\xi_\nu w}{2\pi r_{\mathrm{S\,i}}}\hat{i}_a\sin\left(\nu\alpha-(a-1)\frac{2\pi}{m}\right) \tag{12a}$$

$$A(\alpha, \boldsymbol{i}_k) = -\frac{mw}{\pi r_{\mathrm{S\,i}}}\hat{i}_k\left[\sum_{\nu=gm+k}^{\infty}\xi_\nu\sin\left(\nu\alpha-\omega t-\varphi_{\mathrm{i}\,k}\right)+\sum_{\nu=gm-k>0}^{\infty}\xi_\nu\sin\left(\nu\alpha+\omega t+\varphi_{\mathrm{i}\,k}\right)\right] \quad ; g\in\mathbb{N}_0. \tag{12b}$$

Rotor eccentricities are not taken into account here. However, their influence on the tangential component at the stator bore is also significantly lower than on the radial component of the winding field and can be neglected.

5. Inductances

Using the formulations for the radial airgap winding field density component from section 4.1, the absolute inductances can be calculated. To do so, the formulations for the phase self- and mutual inductances $\boldsymbol{L}_{\mathrm{ph}}$ must first be found, and then transformed into rotor fixed values $\boldsymbol{L}_{\mathrm{dq0}}$. The phase-to-phase inductance L_{ab} consists of two components: $L_{\delta\,ab}$ due to the linkage with the airgap field, and $L_{\sigma\,ab}$ due to the linkage with the leakage field. Like the flux density, the former can be divided into an eccentricity-independent and an eccentricity-dependent component $L_{\delta\,\mathrm{cent}\,ab}$ resp. $L_{\delta\,\mathrm{xy}\,ab}(\boldsymbol{x})$.

$$L_{ab} = L_{\delta\,ab}(\boldsymbol{x}) + L_{\sigma\,ab} = L_{\delta\,\mathrm{cent}\,ab} + L_{\delta\,\mathrm{xy}\,ab}(\boldsymbol{x}) + L_{\sigma\,ab}. \tag{13}$$

5.1. Airgap inductances

The airgap inductance between two phases is calculated in analogy to Eq. (6) using

$$L_{\delta\,ab}(\boldsymbol{x}) = \mu_0 \bar{r}_\delta l_\mathrm{i} \int_0^{2\pi} N_b(\alpha,\boldsymbol{x}) P(\alpha,\boldsymbol{x}) n_a(\alpha)\mathrm{d}\alpha; \qquad a,b \in \{1,2,\ldots,m\}, \tag{14}$$

which leads in conjunction with $\Lambda_\delta = \frac{\mu_0 \bar{r}_\delta l_\mathrm{i} \pi}{k_\mathrm{c} \delta_0'}$ and $\bar{r}_\delta$ as the radius in the middle of the airgap to

$$L_{\delta\,ab}(\boldsymbol{x}) = L_{\delta\,\mathrm{cent}\,ab} + L_{\delta\,\mathrm{xy}\,ab}(\boldsymbol{x}) \tag{15a}$$

$$L_{\delta\,\mathrm{cent}\,ab} = \Lambda_\delta \sum_{\nu=1}^{\infty} \xi_{\mathrm{r}\,\nu} \hat{n}_\nu^2 \cos\left((a-b)\,\nu\frac{2\pi}{m}\right) \tag{15b}$$

$$L_{\delta\,\mathrm{xy}\,ab}(\boldsymbol{x}) = \Lambda_\delta \sum_{\nu=1}^{\infty} \hat{n}_\nu \hat{n}_{\nu+1} \cos\left((a-b)\,\frac{2\nu+1}{2}\,\frac{2\pi}{m}\right)\left[\frac{x}{\delta_0'}\cos\left(\frac{a+b-2}{2}\,\frac{2\pi}{m}\right) + \frac{y}{\delta_0'}\sin\left(\frac{a+b-2}{2}\,\frac{2\pi}{m}\right)\right]. \tag{15c}$$

To obtain the airgap inductances in rotor-fixed coordinates $\boldsymbol{L}_{\delta\,\mathrm{dq0}}$, the inductance matrix $\boldsymbol{L}_{\delta\,\mathrm{ph}}$ needs to be multiplied on the left and right by the transformation matrices $\boldsymbol{T}_{\mathrm{dq0}}$ resp. $\boldsymbol{T}_{\mathrm{dq0}}^{-1}$. This can be expressed for each matrix element as a double sum, and the resulting elongated formulas can be greatly simplified. The **non-zero** elements of the eccentricity-independent inductance component $\boldsymbol{L}_{\delta\,\mathrm{cent}\,\mathrm{dq0}}$ for a dq-system order $k \in \{1,2,\ldots,\lceil m/2\rceil - 1\}$ are:

$$L_{\delta\,\mathrm{cent}\,\mathrm{d}k\mathrm{d}k} = L_{\delta\,\mathrm{cent}\,\mathrm{q}k\mathrm{q}k} = \frac{m}{2}\Lambda_\delta \sum_{\nu=\pm(gm-k)>0}^{\infty} \xi_{\mathrm{r}\,\nu}\,\hat{n}_\nu^2 \qquad ; g \in \mathbb{Z} \tag{16a}$$

$$L_{\delta\,\mathrm{cent}\,\mathrm{q0q0}} = m\Lambda_\delta \sum_{\nu=(2g+1)\frac{m}{2}}^{\infty} \xi_{\mathrm{r}\,\nu}\hat{n}_\nu^2 \qquad ; g \in \mathbb{N}_0. \tag{16b}$$

They form a diagonal matrix, so that there is no coupling between the dq-systems nor within the systems. The **non-zero** elements of the eccentricity-dependent component $\boldsymbol{L}_{\delta\,\mathrm{xy}\,\mathrm{dq0}}$ form 2x2 coupling submatrices between two systems:

$$L_{\delta\,\mathrm{xy}\,\mathrm{d}k\mathrm{d}k+1} = L_{\delta\,\mathrm{xy}\,\mathrm{q}k\mathrm{q}k+1} = \frac{m}{4}\Lambda_\delta \frac{x}{\delta_0'}\left[\sum_{\nu=k-gm>0}^{\infty}\left[\hat{n}_\nu\hat{n}_{\nu+1}\right] + \sum_{\nu=gm-k-1>0}^{\infty}\left[\hat{n}_\nu\hat{n}_{\nu+1}\right]\right] \qquad ; g \in \mathbb{Z} \tag{17a}$$

$$L_{\delta\,\mathrm{xy}\,\mathrm{d}k\mathrm{q}k+1} = -L_{\delta\,\mathrm{xy}\,\mathrm{q}k\mathrm{d}k+1} = \frac{m}{4}\Lambda_\delta \frac{y}{\delta_0'}\left[\sum_{\nu=k-gm>0}^{\infty}\left[\hat{n}_\nu\hat{n}_{\nu+1}\right] + \sum_{\nu=gm-k-1>0}^{\infty}\left[\hat{n}_\nu\hat{n}_{\nu+1}\right]\right] \qquad ; g \in \mathbb{Z}. \tag{17b}$$

If the phase number m is uneven there are also additional eccentricity and angular dependent inductances within the dq-system of highest order $k = (m-1)/2$, as the corresponding MMF spectrum contains forward and backward rotating harmonic waves, which orders differ by one:

$$L_{\delta\,\mathrm{xy}\,\mathrm{d}\frac{m-1}{2}\mathrm{d}\frac{m-1}{2}} = -L_{\delta\,\mathrm{xy}\,\mathrm{q}\frac{m-1}{2}\mathrm{q}\frac{m-1}{2}} = \frac{m}{2}\Lambda_\delta \sum_{\nu=\frac{m-1}{2}+gm}^{\infty}\left[\hat{n}_\nu\hat{n}_{\nu+1}\left[\frac{x}{\delta_0'}\cos(2\theta) - \frac{y}{\delta_0'}\sin(2\theta)\right]\right] \qquad ; g \in \mathbb{N}_0 \tag{18a}$$

$$L_{\delta\,\mathrm{xy}\,\mathrm{d}\frac{m-1}{2}\mathrm{q}\frac{m-1}{2}} = L_{\delta\,\mathrm{xy}\,\mathrm{q}\frac{m-1}{2}\mathrm{d}\frac{m-1}{2}} = -\frac{m}{2}\Lambda_\delta \sum_{\nu=\frac{m-1}{2}+gm}^{\infty}\left[\hat{n}_\nu\hat{n}_{\nu+1}\left[\frac{x}{\delta_0'}\cos(2\theta) + \frac{y}{\delta_0'}\sin(2\theta)\right]\right] \qquad ; g \in \mathbb{N}_0. \tag{18b}$$

There exist also eccentricity and angular dependent inductances for even phase numbers between the homopolar zero component and the dq-system of highest order $k = m/2 - 1$:

$$L_{\delta\,\mathrm{xy}\,\mathrm{d}\frac{m}{2}-1\mathrm{q}0} = \frac{m}{2\sqrt{2}}\Lambda_\delta\left[\frac{x}{\delta_0'}\cos(\theta) - \frac{y}{\delta_0'}\sin(\theta)\right]\left[\sum_{\nu=(2g+1)\frac{m}{2}}^{\infty}\left[\hat{n}_\nu\hat{n}_{\nu+1}\right] + \sum_{\nu=(2g+1)\frac{m}{2}-1}^{\infty}\left[\hat{n}_\nu\hat{n}_{\nu+1}\right]\right] \qquad ; g \in \mathbb{N}_0 \tag{19a}$$

$$L_{\delta\,\mathrm{xy}\,\mathrm{q}\frac{m}{2}-1\mathrm{q}0} = -\frac{m}{2\sqrt{2}}\Lambda_\delta\left[\frac{x}{\delta_0'}\sin(\theta) + \frac{y}{\delta_0'}\cos(\theta)\right]\left[\sum_{\nu=(2g+1)\frac{m}{2}}^{\infty}\left[\hat{n}_\nu\hat{n}_{\nu+1}\right] + \sum_{\nu=(2g+1)\frac{m}{2}-1}^{\infty}\left[\hat{n}_\nu\hat{n}_{\nu+1}\right]\right] \qquad ; g \in \mathbb{N}_0. \tag{19b}$$

5.2. Leakage inductances

The phase-to-phase leakage inductances include the airgap leakage inductance as well as the slot leakage inductance and the necessary permeance factors can be calculated according to (Pyrhönen, Jokinen, and Hrabovcová, 2013). The airgap leakage inductance is already included in the inductance equations above. The end winding leakage inductance for multi-phase machines requires in-depth knowledge about the end winding design and is therefore neglected here.

Starting from the self inductance permeance factors of the bottom and the upper layer $\lambda_{\sigma\,\mathrm{su}}$ resp. $\lambda_{\sigma\,\mathrm{so}}$ as well as the mutual inductance permeance factor $\lambda_{\sigma\,\mathrm{g}}$ and assuming a multi-phase winding scheme with strictly consecutive zones, one can determine the phase-to-phase leakage inductances $\boldsymbol{L}_{\sigma\,\mathrm{ph}}$ by:

$$\boldsymbol{L}_{\sigma\,\mathrm{ph}} = \mu_0 l_\mathrm{i} w_\mathrm{sp}^2 \boldsymbol{\lambda}_{\sigma\,\mathrm{ph}} \tag{20a}$$

$$\begin{aligned}\lambda_{\sigma\,\mathrm{ph}\,i+1,j+1} = {} & \delta_{i,j}\, q\,(\lambda_{\sigma\,\mathrm{so}} + \lambda_{\sigma\,\mathrm{su}}) - \left(\delta_{j,(\iota+i) \bmod m} + \delta_{j,(-\iota+i) \bmod m}\right)(q - (y \bmod q))\lambda_{\sigma\,\mathrm{g}} - \\ & - \left(\delta_{j,(\iota+1+i) \bmod m} + \delta_{j,(-\iota-1+i) \bmod m}\right)(y \bmod q)\lambda_{\sigma\,\mathrm{g}},\end{aligned} \tag{20b}$$

with the Kronecker-Delta $\delta_{i,j}$ and $\iota = \lfloor y/q \rfloor$. Transforming this cyclic matrix into the rotor-oriented coordinate system yields a diagonal matrix $\boldsymbol{L}_{\sigma\,\mathrm{dq0}}$ with the elements:

$$L_{\sigma\,\mathrm{d}k\mathrm{d}k} = L_{\sigma\,\mathrm{q}k\mathrm{q}k} = L_{\sigma\,\mathrm{ph}\,1,1} + 2L_{\sigma\,\mathrm{ph}\,1,1+\iota}\cos\left(\iota k\frac{2\pi}{m}\right) + 2L_{\sigma\,\mathrm{ph}\,1,2+\iota}\cos\left((\iota+1)\,k\frac{2\pi}{m}\right) \tag{21a}$$

$$L_{\sigma\,\mathrm{d0d0}} = L_{\sigma\,\mathrm{ph}\,1,1} + 2L_{\sigma\,\mathrm{ph}\,1,1+\iota} + 2L_{\sigma\,\mathrm{ph}\,1,2+\iota} \tag{21b}$$

$$L_{\sigma\,\mathrm{q0q0}} = L_{\sigma\,\mathrm{ph}\,1,1} + (-1)^{\iota} 2L_{\sigma\,\mathrm{ph}\,1,1+\iota} + (-1)^{\iota+1} 2L_{\sigma\,\mathrm{ph}\,1,2+\iota}. \tag{21c}$$

The derived expressions for the inductances in synchronous coordinates can directly be used as initial values for control system design. Assuming small eccentricities, all dq-systems and both zero components can be controlled separately, as all inductance matrices are diagonal and the coupling inductances are orders of magnitude smaller.

6. Permanent magnet airgap field

The investigated spindle motor has radially magnetized surface permanent magnets. Assuming an equivalent PM-MMF Θ_PM, we can calculate the radial field density component analogously to the winding field density. This allows us to obtain a compact analytical description. The positive magnet axis is aligned with the global x-axis.

6.1. Radial flux density

Analogous to Eq. (6), we obtain for the radial flux density via the equivalent MMF:

$$\Theta_\mathrm{PM}(\alpha,\omega t) = \sum_{\nu=1}^{\infty}\hat{\Theta}_{\mathrm{PM}\,\nu/p}\cos\left(\nu\alpha - \frac{\nu}{p}\omega t\right) = \sum_{\nu=1}^{\infty}\frac{4}{\pi}\frac{B_{\mathrm{rem\,PM}}}{\mu_0\mu_{\mathrm{r\,PM}}}h_\mathrm{PM}\frac{\sin\left(\alpha_\mathrm{p}\frac{\nu}{p}\frac{\pi}{2}\right)}{\nu/p}\cos\left(\nu\alpha - \frac{\nu}{p}\omega t\right) \tag{22a}$$

$$\begin{aligned}B_{\mathrm{PM\,r}}(\alpha,\omega t,\boldsymbol{x}) = B_{\mathrm{PM\,r\,cent}}(\alpha,\omega t) + B_{\mathrm{PM\,r\,xy}}(\alpha,\omega t,\boldsymbol{x}) = {} & \frac{\mu_0}{k_\mathrm{c}\delta_0'}\sum_{\nu=1}^{\infty}\hat{\Theta}_{\mathrm{PM}\,\nu/p}\Bigg[\cos\left(\nu\alpha - \frac{\nu}{p}\omega t\right) + \\ & + \frac{x}{2\delta_0'}\left[\cos\left(\alpha(\nu-1) - \frac{\nu}{p}\omega t\right) + \cos\left(\alpha(\nu+1) - \frac{\nu}{p}\omega t\right)\right] + \frac{y}{2\delta_0'}\left[-\sin\left(\alpha(\nu-1) - \frac{\nu}{p}\omega t\right) + \sin\left(\alpha(\nu+1) - \frac{\nu}{p}\omega t\right)\right]\Bigg].\end{aligned} \tag{22b}$$

6.2. Flux linkage

The corresponding PM flux linkage can be calculated by integrating the product of the flux linkage and the winding function over the airgap. Afterwards, the transformation into the rotor-oriented coordinate system leads to:

$$\Psi_{\mathrm{PM\,cent\,d}k} = \Lambda_\delta \sum_{\nu=gm+k}^{\infty}\hat{\Theta}_{\mathrm{PM}\,|\nu/p|}\hat{n}_{|\nu|}\cos\left(\left(\frac{\nu}{p}-1\right)\omega t\right) \qquad ;g\in\mathbb{Z} \tag{23a}$$

$$\Psi_{\mathrm{PM\,cent\,q}k} = \Lambda_\delta \sum_{\nu=gm+k}^{\infty}\hat{\Theta}_{\mathrm{PM}\,|\nu/p|}\hat{n}_{|\nu|}\sin\left(\left(\frac{\nu}{p}-1\right)\omega t\right) \qquad ;g\in\mathbb{Z} \tag{23b}$$

$$\Psi_{\mathrm{PM\,cent\,q0}} = \sqrt{2}\Lambda_\delta \sum_{\nu=(2g+1)m/2}^{\infty}\hat{\Theta}_{\mathrm{PM}\,\nu/p}\hat{n}_\nu\cos\left(\frac{\nu}{p}\omega t\right) \qquad ;g\in\mathbb{N}_0. \tag{23c}$$

Same as for the inductances, the derived flux linkages can be used as a starting point for control system design. In case of an even phase number, special attention needs to be put on the angular dependent flux linkage component $\Psi_{\mathrm{PM\,cent\,q0}}$.

7. Torque and Force

For the mechanical description of the motor, expressions for the torque and the radial forces are required. These are derived according Eq. (4) using Maxwell's stress tensor and the equations for the flux densities resp. flux linkages above. We assume the superposition of the fundamental motor current system $\boldsymbol{i}_\mathrm{m}$ and the fundamental suspension current system $\boldsymbol{i}_\mathrm{s}$ of order $k = p$ resp. $k = p_\mathrm{s}$ and neglect the tangential component of the PM field in the whole section. Then there is only torque generation due to the interaction of the radial component of the PM field and the tangential component of the motor field for motors without reluctance differences in the rotor. We can express the airgap torque T_i therefore by the q-axis motor current i_qm and the PM flux linkage for a centered rotor in the same dq-system:

$$T_\mathrm{i} = \frac{m}{2} i_\mathrm{qm} \sum_{\nu=gm+p}^{\infty} \nu \, \hat{\Psi}_{\mathrm{PM\,cent\,dm}\,|\nu|} \cos\left(\left(\frac{\nu}{p} - 1\right)\omega t\right) \qquad ; g \in \mathbb{Z}. \tag{24}$$

Force generation is more complex to describe than torque generation as there can interact two radial field components as well a radial and a tangential one, see Eq. (4). Assuming linear relationships, the force consists out of a component for a centered rotor $\boldsymbol{F}_\mathrm{cent}$ and a component from the eccentricity $\boldsymbol{F}_\mathrm{ecc}$ (indices: $F_{\mathrm{cent/ecc\ field\ 1,\ field\ 2,\ rad./tan.\ of\ field\ 1,\ rad./tan.\ of\ field\ 2}}$).

$$\boldsymbol{F} = \boldsymbol{F}_\mathrm{cent} + \boldsymbol{F}_\mathrm{ecc} \tag{25a}$$

$$\boldsymbol{F}_\mathrm{cent} = \boldsymbol{F}_\mathrm{cent\,PM\,m\,rr} + \boldsymbol{F}_\mathrm{cent\,PM\,s\,rr} + \boldsymbol{F}_\mathrm{cent\,m\,s\,rr} + \boldsymbol{F}_\mathrm{cent\,PM\,m\,rt} + \boldsymbol{F}_\mathrm{cent\,PM\,s\,rt} + \boldsymbol{F}_\mathrm{cent\,m\,s\,rt} + \boldsymbol{F}_\mathrm{cent\,s\,m\,rt} \tag{25b}$$

$$\boldsymbol{F}_\mathrm{ecc} = \boldsymbol{F}_\mathrm{ecc\,PM\,PM\,rr} + \boldsymbol{F}_\mathrm{ecc\,m\,m\,rr} + \boldsymbol{F}_\mathrm{ecc\,s\,s\,rr} + \boldsymbol{F}_\mathrm{ecc\,PM\,m\,rr} + \boldsymbol{F}_\mathrm{ecc\,PM\,s\,rr} \tag{25c}$$

PM-field and motor field: The motor field waves of the orders $\nu = |gm + p|$, $g \in \mathbb{Z}$ interact with the forward rotating PM field waves that deviate by one order. For the force in x- resp. y-direction due to the interactions of radial and tangential components, we get with $\Delta\varphi = 0$ resp. $\Delta\varphi = \pi/2$:

$$\begin{aligned}
F_{\mathrm{cent\,PM\,m\,x/y}} = \frac{m}{4}\Bigg[& \sum_{\nu=gm+p}^{\infty} \Bigg[\hat{\Psi}_{\mathrm{PM\,dp}\,\nu-1} \frac{\hat{n}_\nu}{\hat{n}_{\nu-1}} \left(\frac{\xi_{\mathrm{r}\,\nu}}{k_\mathrm{c}\delta_0'} + \frac{\nu}{r_\mathrm{Si}}\right) \left(\cos\left(\left(1 - \frac{\nu-1}{p}\right)\omega t - \Delta\varphi\right) i_\mathrm{dm} - \sin\left(\left(1 - \frac{\nu-1}{p}\right)\omega t - \Delta\varphi\right) i_\mathrm{qm}\right) + \\
& + \hat{\Psi}_{\mathrm{PM\,dp}\,\nu+1} \frac{\hat{n}_\nu}{\hat{n}_{\nu+1}} \left(\frac{\xi_{\mathrm{r}\,\nu}}{k_\mathrm{c}\delta_0'} - \frac{\nu}{r_\mathrm{Si}}\right) \left(\cos\left(\left(1 - \frac{\nu+1}{p}\right)\omega t + \Delta\varphi\right) i_\mathrm{dm} - \sin\left(\left(1 - \frac{\nu+1}{p}\right)\omega t + \Delta\varphi\right) i_\mathrm{qm}\right) \Bigg] + \\
& + \sum_{\nu=gm-p>0}^{\infty} \Bigg[\hat{\Psi}_{\mathrm{PM\,dp}\,\nu-1} \frac{\hat{n}_\nu}{\hat{n}_{\nu-1}} \left(\frac{\xi_{\mathrm{r}\,\nu}}{k_\mathrm{c}\delta_0'} + \frac{\nu}{r_\mathrm{Si}}\right) \left(\cos\left(\left(1 + \frac{\nu-1}{p}\right)\omega t + \Delta\varphi\right) i_\mathrm{dm} - \sin\left(\left(1 + \frac{\nu-1}{p}\right)\omega t + \Delta\varphi\right) i_\mathrm{qm}\right) + \\
& + \hat{\Psi}_{\mathrm{PM\,dp}\,\nu+1} \frac{\hat{n}_\nu}{\hat{n}_{\nu+1}} \left(\frac{\xi_{\mathrm{r}\,\nu}}{k_\mathrm{c}\delta_0'} - \frac{\nu}{r_\mathrm{Si}}\right) \left(\cos\left(\left(1 + \frac{\nu+1}{p}\right)\omega t - \Delta\varphi\right) i_\mathrm{dm} - \sin\left(\left(1 + \frac{\nu+1}{p}\right)\omega t - \Delta\varphi\right) i_\mathrm{qm}\right) \Bigg] \Bigg].
\end{aligned} \tag{26}$$

The equation above only describes force ripple, as the PM flux linkage appears in the dq-system of order p and possibly in the homopolar zero component. Therefore, it can be seen that there is no force effect for the fundamental wave.

PM-field and suspension field: The formula for $\boldsymbol{F}_{\mathrm{cent\,PM\,s\,x/y}}$ is not stated specifically. It is analogous to the equation above as suspension field waves of the orders $\nu = |gm + p_\mathrm{s}|$, $g \in \mathbb{Z}$ interact with the forward rotating PM field waves that deviate by one order. In this case there is a constant force for the fundamental wave.

Motor and suspension field: All forward rotating motor field waves of the orders $\nu = gm + p$ interact with the forward rotating damping field waves of the orders $\nu = gm + p_\mathrm{s}$ $g \in \mathbb{N}_0$. The same applies to the backward rotating field waves. There is no interaction between field waves rotating in opposite directions and therefore just constant force generation.

$$\begin{aligned}
\begin{bmatrix} F_{\mathrm{cent\,m\,s\,x}} \\ F_{\mathrm{cent\,m\,s\,y}} \end{bmatrix} = \frac{m^2}{8} \frac{\pi\mu_0 l_\mathrm{i}}{k_\mathrm{c}\delta_0'} \begin{bmatrix} i_\mathrm{dm} i_\mathrm{ds} + i_\mathrm{qm} i_\mathrm{qs} \\ \pm i_\mathrm{dm} i_\mathrm{qs} \mp i_\mathrm{qm} i_\mathrm{ds} \end{bmatrix} \Bigg[& \sum_{\nu=gm+p}^{\infty} \left[\hat{n}_\nu \hat{n}_{\nu\pm1} \left(\frac{r_\mathrm{Si}}{k_\mathrm{c}\delta_0'} \xi_{\mathrm{r}\,\nu} \xi_{\mathrm{r}\,\nu\pm1} \pm \xi_{\mathrm{r}\,\nu}(\nu \pm 1) \mp \xi_{\mathrm{r}\,\nu\pm1}\nu \right) \right] + \\
& + \sum_{\nu=gm-p>0}^{\infty} \left[\hat{n}_\nu \hat{n}_{\nu\mp1} \left(\frac{r_\mathrm{Si}}{k_\mathrm{c}\delta_0'} \xi_{\mathrm{r}\,\nu} \xi_{\mathrm{r}\,\nu\mp1} \mp \xi_{\mathrm{r}\,\nu}(\nu \mp 1) \pm \xi_{\mathrm{r}\,\nu\mp1}\nu \right) \right] \Bigg],
\end{aligned} \tag{27}$$

The alternating ±-signs stand for $p_\mathrm{s} = p \pm 1$.

In the special case of an odd number of phases and the choices $p = (m-1)/2$ or $p_\mathrm{s} = (m-1)/2$, in addition to the forward-rotating motor or damping field waves, there are also backward-rotating field waves that are always one order higher. This results in a force ripple of double the fundamental frequency. Such a pole-phase combination should therefore be avoided.

$$F_{\mathrm{cent\,m\,m\,rr\,x/y}} = \frac{m^2}{8} \frac{\pi\mu_0 l_\mathrm{i} r_\mathrm{Si}}{k_\mathrm{c}^2 \delta_0'^2} \sum_{\nu=gm+\frac{m-1}{2}}^{\infty} \left[\hat{n}_\nu \hat{n}_{\nu+1} \xi_{\mathrm{r}\,\nu} \xi_{\mathrm{r}\,\nu+1} \left(\cos(2\omega t + \Delta\varphi) \left(i_\mathrm{dm}^2 - i_\mathrm{qm}^2\right) - \sin(2\omega t + \Delta\varphi) 2 i_\mathrm{dm} i_\mathrm{qm} \right) \right] \tag{28}$$

PM-field: In case of a rotor eccentricity the additional harmonics whose orders differ by one from the existing harmonics, see Eq. (22b), lead to additional force generation. Due to the approximation of the inverse airgap length by means of a first order Taylor expansion, the force in the x- or y-direction depends only on the eccentricity in the same direction.

$$\begin{bmatrix} F_{\mathrm{ecc\,PM\,PM\,rr\,x}} \\ F_{\mathrm{ecc\,PM\,PM\,rr\,y}} \end{bmatrix} = \frac{1}{2\pi\mu_0 l_\mathrm{i} r_\mathrm{Si}} \frac{1}{\delta_0'} \begin{bmatrix} x \\ y \end{bmatrix} \cdot \sum_{\nu=1}^{\infty} \frac{\hat{\Psi}^2_{\mathrm{PM\,dp}\,\nu}}{\hat{n}_\nu^2} \tag{29}$$

Motor resp. suspension field: As for the PM field, there are also additional harmonics for the motor and damping fields due to the eccentric rotor position with orders deviating by one. Only field waves with the same direction of rotation interact. The resulting forces are exemplary for the motor field:

$$\begin{bmatrix} F_{\mathrm{ecc\,m\,m\,rr\,x}} \\ F_{\mathrm{ecc\,m\,m\,rr\,y}} \end{bmatrix} = \frac{m^2}{8} \frac{\pi\mu_0 l_\mathrm{i} r_\mathrm{Si}}{k_\mathrm{c}^2 \delta_0'^2} \frac{1}{\delta_0'} \begin{bmatrix} x \\ y \end{bmatrix} \cdot \left[\sum_{\nu=gm+p}^{\infty} \left[\xi_{\mathrm{r}\,\nu} \hat{n}_\nu^2 \left(1 - \frac{\delta_{1,\nu}}{2} \right) \right] + \sum_{\nu=gm-p>0}^{\infty} \left[\xi_{\mathrm{r}\,\nu} \hat{n}_\nu^2 \right] \right] \left(i_\mathrm{dm}^2 + i_\mathrm{qm}^2 \right). \tag{30}$$

PM-field and motor field: Numerous interactions are possible between the PM field and the motor field. The additional harmonics of the PM field can interact with the harmonics of the motor field for the rotor in center position and vice versa, regardless of the direction of rotation. The force effects in the x and y directions are, with $g \in \mathbb{Z}$:

$$\begin{bmatrix} F_{\mathrm{ecc\,PM\,m\,rr\,x}} \\ F_{\mathrm{ecc\,PM\,m\,rr\,y}} \end{bmatrix} = \frac{m}{4} \frac{1}{k_\mathrm{c} \delta_0'^2} \begin{bmatrix} x \\ y \end{bmatrix} \cdot \sum_{\nu=gm+p}^{\infty} \left[(1 + \xi_{\mathrm{r}\,|\nu|})\, \hat{\Psi}_{\mathrm{PM\,dp}\,|\nu|} \left[i_\mathrm{dm} \cos\left(\left(1 - \frac{\nu}{p} \right) \omega t \right) - i_\mathrm{qm} \sin\left(\left(1 - \frac{\nu}{p} \right) \omega t \right) \right] \right]. \tag{31}$$

All torque and force expressions from above can be rearranged to determine fundamental design parameters, like r_Si, l_i, $\hat{A}_1$, $\hat{B}_{\mathrm{PM\,r\,1}}$, but also to identify critical harmonics and corresponding winding factors when force or torque ripple requirements need to be met.

8. Validation against FEM-Simulation

To validate the derived formulas from the sections above, 2D-FEM simulations in "ANSYS Maxwell" have been performed. The linear cases consider a relative permeability of the steel material of $\mu_{\mathrm{r\,Fe}} = 10^7$, as the magnetic voltage drop in the iron is neglected in the motor model, while the non-linear cases consider the actual B-H-curve of the material. Simulations regarding the PM-field are conducted at no-load, all other simulations are conducted at the arbitrary operating point: $i_\mathrm{dm} = -0.62\,\mathrm{A}$, $i_\mathrm{qm} = 9.7\,\mathrm{A}$, $i_\mathrm{ds} = -7.45\,\mathrm{A}$, $i_\mathrm{qs} = -6.25\,\mathrm{A}$.

PM field: The calculation of the PM flux density via an equivalent PM-MMF Θ_PM, see Eq. (22a), leads to a significant overestimation as Fig. 1 shows. The relative deviation of the fundamental wave amplitude is 8 % compared to the linear FEM and 10.3 % compared to the nonlinear FEM. This is due to the large mechanical airgap. Equation (22) does not consider any radial dependency and appears to be valid only at the magnet surface. Thus, the PM flux density and linkage are also calculated using the 2D magnetic scalar potential, as in (Rahideh and Korakianitis, 2011), and are then compared to the FEM results. Except for the unaccounted slotting effect, the accuracy is high, with a deviation of around 3 % for the first two harmonics in the nonlinear case. The flux linkages on the right side of Fig. 1 support these results.

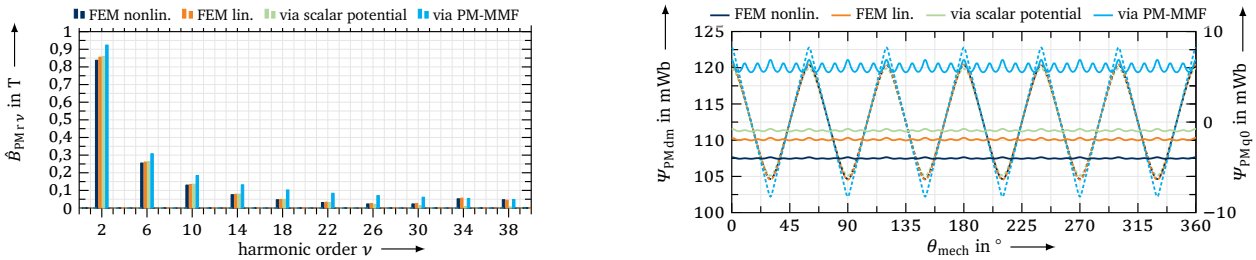

Fig. 1: Simulated and calculated PM field quantities at no-load for a centered rotor: (left) amplitude spectrum of the flux density at the stator bore; (right) flux linkages $\Psi_{\mathrm{PM\,dm}}$ (solid) and $\Psi_{\mathrm{PM\,q0}}$ (dashed) over one mechanical revolution

Winding field: Since the inductances are calculated directly from the radial airgap winding field, they are used to validate the corresponding formulas in Sections 4 and 5. Table 2 lists the relevant values for an eccentricity of 50 µm, as this is the maximum expected during the later damping operation in the milling spindle. The calculations and simulations agree well with relative deviations of max. 4.3 % for all relevant airgap inductances and max. 16 % for the leakage inductances. They confirm the above statement regarding the separately controllable dq-systems. The simulated airgap inductances are determined based on the flux density at the middle of the airgap and the respective winding functions. It is not feasible to compare the eccentricity-dependent coupling inductances to the nonlinear FEM because these are non-zero even when the rotor is centered. However, a differential calculation yields values similar to those in the linear case.

Table 2: Simulated and calculated inductances for a rotor eccentricity of $x = 50\,\mu\text{m}$

inductance	FEM nonlin.	FEM lin.	analytical	inductance	FEM nonlin.	FEM lin.	analytical
$L_{\delta\,\text{cent d1d1}}$	3.02 mH	3.15 mH	3.06 mH	$L_{\sigma\,\text{d1d1}}$	236 µH	245 µH	273 µH
$L_{\delta\,\text{cent d2d2}}$	1.98 mH	2.03 mH	1.97 mH	$L_{\sigma\,\text{d2d2}}$	493 µH	507 µH	578 µH
$L_{\delta\,\text{cent d3d3}}$	0.882 mH	0.896 mH	0.867 mH	$L_{\sigma\,\text{d3d3}}$	498 µH	507 µH	578 µH
$L_{\delta\,\text{cent d4d4}}$	0.237 mH	0.241 mH	0.232 mH	$L_{\sigma\,\text{d4d4}}$	326 µH	332 µH	375 µH
$L_{\delta\,\text{cent d5d5}}$	0.0750 mH	0.0772 mH	0.0739 mH	$L_{\sigma\,\text{d5d5}}$	238 µH	245 µH	273 µH
$L_{\delta\,\text{cent q0q0}}$	0.0836 mH	0.0858 mH	0.0822 mH	$L_{\sigma\,\text{q0q0}}$	238 µH	245 µH	273 µH
$L_{\delta\,\text{xy d1d2}}$	—	11 µH	11.2 µH	$L_{\delta\,\text{xy d2d3}}$	—	5.48 µH	5.81 µH

Torque and Force: The mean torque differs by 0.3 % for the linear FEM, when considering a 2D PM field density whereas a calculation via the PM-MMF leads to an error of 8.1 %. The higher harmonic effects are also represented well, except for the not modeled slotting harmonics. For the nonlinear FEM, the relative deviations increase to 3.7 % resp. 11.8 %. The torque can be considered as eccentricity-independent as the ripple only increases from 2.8 % to 3.4 %. Compared to the nonlinear FEM, force deviations seem to be larger than torque deviations. Indeed, the force vector magnitude differs by 0.4 % (linear) resp. 18.4 % (nonlin.), but the deviations appear even larger due to the angular errors of 3° resp. 4.7°, caused by higher harmonic components. A fundamental approach reduces the angular error but increases the magnitude error. Force shows greater eccentricity dependence, with ripple increasing from 1.4 % to 6.9 %. For force control, rotor eccentricity should be incorporated when eccentricities of several tenths of a millimeter are expected.

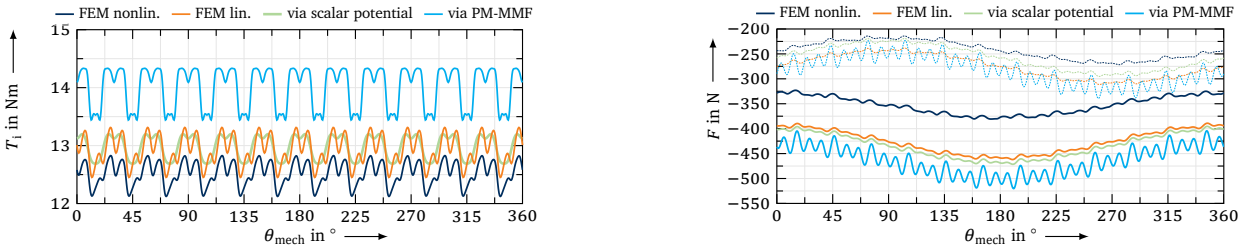

Fig. 2: Simulated and calculated mechanical quantities at the operation point: (left) torque for centered rotor; (right) force in x- (solid) and y-direction (dashed) for a dynamic eccentricity of 50 µm

9. Conclusion

Multi-phase bearingless machines offer the ability of a highly flexible simultaneous force and torque generation at the cost of increased system complexity. This paper offers a compact linear analytical model in stationary and synchronous coordinates considering higher harmonics and rotor eccentricity with good matches to corresponding FEM simulations. Due to the large airgap in surface PMSM, 2D-modeling of the magnetic fields should be used. Rearranging the equations also makes them usable to identify design parameters when force and torque requirements are given. The model parameters in synchronous coordinates can serve as starting values for the control design.

References

Faiz, J. and I. Tabatabaei (2002). “Extension of winding function theory for nonuniform air gap in electric machinery”. In: *IEEE Transactions on Magnetics* 38(6), pp. 3654–3657.

Guhl, D. and W. Hofmann (2024). “Design of Multi-Phase Combined Windings for Bearingless Machines with Focus on Higher Harmonic Effects”. In: *2024 International Symposium on Power Electronics, Electrical Drives, Automation and Motion (SPEEDAM)*, pp. 25–31.

Guhl, D., R. Liebfried, and W. Hofmann (2021). “Design and Comparison of Dual-Purpose Stator Windings for Active Chatter Suppression in Milling Spindles”. In: *17th International Symposium on Magnetic Bearings*, pp. 237–251.

Khamitov, A. and E. L. Severson (2025). “Multiharmonic Force Vector Model for Bearingless Electric Motors”. In: *IEEE Transactions on Industry Applications* 61(1), pp. 231–242.

Loewenherz, R. H. et al. (2020). “Modeling of Modular Multi-Phase Machines”. In: *2020 23rd International Conference on Electrical Machines and Systems (ICEMS)*, pp. 559–564.

Pyrhönen, J., T. Jokinen, and V. Hrabovcová (2013). *Design of rotating electrical machines*. John Wiley & Sons.

Rahideh, A. and T. Korakianitis (2011). “Analytical Open-Circuit Magnetic Field Distribution of Slotless Brushless Permanent-Magnet Machines With Rotor Eccentricity”. In: *IEEE Transactions on Magnetics* 47(12), pp. 4791–4808.

Zhu, Z. and D. Howe (1993). “Instantaneous magnetic field distribution in brushless permanent magnet DC motors. II. Armature-reaction field”. In: *IEEE Transactions on Magnetics* 29(1), pp. 136–142.